



HAL
open science

Effect of a Magnetospheric Compression on Jovian Radio Emissions: In Situ Case Study Using Juno Data

C K Louis, C M Jackman, G. Hospodarsky, A. O'kane Hackett, E. Devon-Hurley, P. Zarka, W S Kurth, R W Ebert, D M Weigt, A R Fogg, et al.

► To cite this version:

C K Louis, C M Jackman, G. Hospodarsky, A. O'kane Hackett, E. Devon-Hurley, et al.. Effect of a Magnetospheric Compression on Jovian Radio Emissions: In Situ Case Study Using Juno Data. Journal of Geophysical Research Space Physics, 2023, 128 (9), 10.1029/2022JA031155 . hal-04225345

HAL Id: hal-04225345

<https://hal.sorbonne-universite.fr/hal-04225345>

Submitted on 2 Oct 2023

HAL is a multi-disciplinary open access archive for the deposit and dissemination of scientific research documents, whether they are published or not. The documents may come from teaching and research institutions in France or abroad, or from public or private research centers.

L'archive ouverte pluridisciplinaire **HAL**, est destinée au dépôt et à la diffusion de documents scientifiques de niveau recherche, publiés ou non, émanant des établissements d'enseignement et de recherche français ou étrangers, des laboratoires publics ou privés.

Effect of a magnetospheric compression on Jovian radio emissions: in situ case study using Juno data

C. K. Louis^{1,2}, C. M. Jackman¹, G. Hospodarsky³, A. O’Kane Hackett^{1,4},
E. Devon-Hurley^{1,4}, P. Zarka^{2,5}, W. S. Kurth³, R. W. Ebert^{6,7}, D. M. Weigt^{1,8},
A. R. Fogg¹, J. E. Waters⁹, S. C. McEntee^{1,4}, J. E. P. Connerney¹⁰,
P. Louarn¹¹, S. Levin¹², S. J. Bolton⁶

¹School of Cosmic Physics, DIAS Dunsink Observatory, Dublin Institute for Advanced Studies, Dublin 15, Ireland

²Observatoire Radioastronomique de Nançay, Observatoire de Paris, Université PSL, CNRS, University Orléans, Nançay, France

³Department of Physics and Astronomy, University of Iowa, Iowa City, Iowa, USA

⁴School of Physics, Trinity College Dublin, Dublin, Ireland

⁵LESIA, Observatoire de Paris, PSL Research University, CNRS, Sorbonne Université, UPMC University Paris 06, University Paris Diderot, Sorbonne Paris Cité, Meudon, France

⁶Southwest Research Institute, San Antonio, Texas, USA

⁷Department of Physics and Astronomy, University of Texas at San Antonio, San Antonio, Texas, USA

⁸Department of Computer Science, Aalto University, Aalto, Finland

⁹Department of Physics and Astronomy, University of Southampton, Highfield Campus, Southampton, SO17 1BJ, UK

¹⁰Space Research Corporation, Annapolis, MD

¹¹IRAP, Université de Toulouse, CNRS, CNES, UPS, Toulouse, France

¹²Jet Propulsion Laboratory, Pasadena, California, USA

Key Points:

- This paper provides a list of the Jovian magnetosphere boundary crossings by the Juno spacecraft from June 2016 to August 2022.
- Jovian magnetospheric compressions lead to increased bKOM radio emissions (immediately) and DAM on the dusk sector (more than one rotation later).
- nKOM radio emission appears later during relaxation phase of the compression.

Corresponding author: Corentin Kenelm Louis, corentin.louis@dias.ie

29 **Abstract**

30 During its polar orbits around Jupiter, Juno often crosses the boundaries of the
 31 Jovian magnetosphere (namely the magnetopause and bow shock). From the boundary
 32 locations, the upstream solar wind dynamic pressure can be inferred, which in turn il-
 33 lustrates the state of compression or relaxation of the system. The aim of this study is
 34 to examine Jovian radio emissions during magnetospheric compressions, in order to de-
 35 termine the relationship between the solar wind and Jovian radio emissions. In this pa-
 36 per, we give a complete list of bow shock and magnetopause crossings (from June 2016
 37 to August 2022), and the associated solar wind dynamic pressure and standoff distances
 38 inferred from Joy et al. (2002). We then select two sets of magnetopause crossings with
 39 moderate to strong compression of the magnetosphere for two case studies of the response
 40 of the Jovian radio emissions. We confirm that magnetospheric compressions lead to the
 41 activation of new radio sources. Newly-activated broadband kilometric emissions are ob-
 42 served almost simultaneously with compression of the magnetosphere, with sources cov-
 43 ering a large range of longitudes. Decametric emission sources are seen to be activated
 44 more than one rotation later only at specific longitudes and dusk local times. Finally,
 45 the activation of narrowband kilometric radiation is not observed until the magnetosphere
 46 is in its expansion phase.

47 **Plain Language Summary**48 **1 Introduction**

49 Planetary studies often face the challenge of interpreting *in situ* spacecraft obser-
 50 vations without the benefit of an upstream monitor revealing the prevailing conditions
 51 in the interplanetary medium. This is particularly true of the outer planets. Radio emis-
 52 sions provide a direct probe of the site of particle acceleration and have potential to be
 53 used as a proxy for magnetospheric dynamics (see e.g., Cecconi et al. (2022) for Saturn;
 54 Fogg et al. (2022) for Earth). At Jupiter, the radio spectrum is composed of at least six
 55 components, from low-frequency emissions, such as quasi-periodic (QP) bursts or trapped
 56 continuum radiation (from a few kHz to 10s of kHz), up to decametric (DAM) emissions
 57 ranging from a few MHz to 40 MHz (Gurnett & Scarf, 1983; Zarka, 1998; C. K. Louis
 58 et al., 2021a).

59 In this study, we focus on three types of radio emissions observable with Juno: nar-
 60 rowband kilometric (nKOM), broadband kilometric (bKOM) and auroral DAM emis-
 61 sions (i.e., not induced by Galilean moons). The nKOM is attributed to a mode conver-
 62 sion mechanism producing emissions inside Io’s torus at or near the local electron plasma
 63 frequency (Barbosa, 1982; Gurnett & Scarf, 1983; Jones, 1988; Ronnmark, 1992). The
 64 last two components (bKOM and DAM) are auroral emissions, produced by the cyclotron
 65 maser instability (CMI), near the local electron cyclotron frequency. The sources of these
 66 emissions are located on magnetic field lines of magnetic apex (M-Shell) between 10 and
 67 60 (unitless distance of the magnetic field line at the magnetic equator normalized to Jo-
 68 vian radius 71492 km). These emissions are very anisotropic and beamed along the edges
 69 of a hollow cone with an opening of $\sim 75^\circ \pm 5^\circ$ to $\sim 90^\circ$ with respect to the local mag-
 70 netic field lines (Ladreiter et al., 1994; Zarka, 1998; Treumann, 2006; Louarn et al., 2017,
 71 2018; Imai et al., 2019; C. K. Louis, Prangé, et al., 2019).

72 The relation of the different components of Jupiter’s radio emissions to both in-
 73 ternal and external drivers is complex, as shown by several previous studies. These stud-
 74 ies show a relationship between some of the components and external (solar wind) or in-
 75 ternal (rotation, magnetic reconfiguration) drivers. Recently, Zarka et al. (2021) have
 76 re-analyzed data from Cassinis flyby of Jupiter, and found that hectometric (HOM) and
 77 DAM emissions are dominantly rotation-modulated (i.e. emitted from lighthouse-like sources
 78 fixed in Jovian longitude), whereas bKOM is modulated more strongly by the solar wind

79 than by the rotation (i.e. emitted from sources more active within a given Local Time
 80 sector). This last study extends earlier results by Zarka and Genova (1983); Genova et
 81 al. (1987); Imai et al. (2008, 2011). Louarn et al. (1998), using Galileo radio observations,
 82 have shown a sudden onset, and increased intensity (up to $2 \times 10^{-7} \text{ V.m}^{-1}.\text{Hz}^{-1/2}$ at
 83 5 MHz) of bKOM and DAM radio emissions, as well as the activation of new nKOM ra-
 84 dio emissions, during periods of magnetospheric disturbance. They postulated large-scale
 85 energetic events as reconfigurations of the magnetosphere and plasmashet somewhat
 86 analogous to terrestrial substorms. The results obtained by Echer et al. (2010), using
 87 Ulysses spacecraft data during the distant Jupiter encounter and Nançay Decameter Ar-
 88 ray (NDA) data, show that non-Io DAM radio emissions occur during intervals of en-
 89 hanced solar wind dynamic pressure, but without any direct correlation between the emis-
 90 sion duration or power versus the solar wind pressure or the interplanetary shock Mach
 91 number. Using 50 days of observations from Cassini and Galileo, Gurnett et al. (2002)
 92 showed that HOM emissions were triggered by the arrival of interplanetary shocks at Jupiter.
 93 Hess et al. (2012, 2014) have also shown that an increase of the solar wind pressure af-
 94 fects the non-Io-DAM radio emissions, using ground-based radio measurements (Hess
 95 et al., 2012) and Cassini and Galileo radio and magnetic measurements (Hess et al., 2014).
 96 These two studies have compared the type of shocks with the region of source activa-
 97 tion. There are two type of shocks (Kilpua et al., 2015): fast forward shocks (FFS) and
 98 fast reverse shocks (FRS). These shocks are driven by solar coronal mass ejections (CME)
 99 or corotating interaction regions (CIR). The sudden explosion of a CME, at a higher ve-
 100 locity than the ambient solar wind, usually drives a FFS. As this fast CME expands into
 101 the solar system and overtakes the slower background solar wind, a compressed inter-
 102 action region is usually formed, which is delimited by FFS on one side and FRS on the
 103 other side (Smith & Wolfe, 1976; Tsurutani et al., 2006). A FFS is characterized by a
 104 sharp or discontinuous increase of the solar wind velocity, density, temperature and mag-
 105 netic field amplitude. A FRS is characterized by an increase of the solar wind velocity,
 106 but a decrease of the solar wind temperature, density and magnetic field amplitude. Both
 107 Hess et al. (2012, 2014) studies have shown that FFS trigger mostly dusk emissions, whereas
 108 FRS trigger both dawn and dusk emissions, with a time delay depending on the strength/direction
 109 of the interplanetary magnetic field (IMF). All the shock-triggered radio sources were
 110 found to sub-corotate (i.e. rotating slower than the rotation period of Jupiter) with a
 111 rate ranging from 50% to 80% depending on the intensity of the IMF. These rates could
 112 respectively correspond to the extended and compressed states of the Jovian magneto-
 113 sphere.

114 The above cited studies relied on sparse datasets (flybys or remote measurements)
 115 but the once-in-a-generation Juno dataset gives the opportunity for longer-term mon-
 116 itoring of the Jovian system and its radio response. In particular, the apojoves early in
 117 the mission, which took Juno out to radial distances of $\sim 110 R_J$ on the dawn side, place
 118 the spacecraft near the nominal magnetopause and bow shock locations, and afford the
 119 opportunity to sample snippets of in situ solar wind, as well as to determine the posi-
 120 tions of the magnetospheric boundaries at various points in time. All the while, the Juno
 121 radio instrument is constantly monitoring the Jovian radio spectrum. In this study we
 122 utilise this unique dataset to explore the connection between the solar wind and Jupiter's
 123 radio emissions by presenting the first case study of its kind.

124 Section 2 describes the datasets and processing methodology. Section 3 presents
 125 case studies of the Jovian radio emission response to two moderate to strong magneto-
 126 spheric compressions inferred from multiple magnetopause crossings while Juno is on the
 127 outbound leg of its trajectory. Finally in Section 4, we summarise and discuss the re-
 128 sults of this study and present the perspectives.

129

2 Methodology

130

131

132

133

134

135

136

137

138

139

140

141

142

143

144

145

146

147

148

Since July 2016, Juno has been in orbit around Jupiter, making a polar orbit every 53 days during its prime mission. Since the Ganymede flyby in June 2021, the orbits have been shortened to 43 days, before being reduced to 38 days in September 2022 with the Europa flyby. During its first 44 orbits, with an apojoive of up to $\sim 110 R_J$, Juno crossed the boundaries of the magnetosphere several times (Hospodarsky et al., 2017; Ranquist et al., 2019; Montgomery et al., 2022; Collier et al., 2020), as shown in Figure 1 projected into the equatorial plane. Figure 1a displays the magnetopause crossings while Figure 1b displays the bow shock crossings. In both of these panels are drawn the 10th and 90th quantile position of the magnetopause and bow shock, respectively, based on the Joy et al. (2002) model. Note that this model was built on crossings from Ulysses, Voyager and Galileo, and thus may not be representative of all local times (especially the previously poorly explored dusk flank) or high-latitudes. The coordinate system used in this figure is the Juno-de-Spun-Sun (JSS), as this is the coordinate system used in the Joy et al. (2002) model. In this system, X points towards the Sun, Z is aligned with the Jovian spin axis, and Y closes the right-handed system (positive towards dusk). A 3D projection plot (in the Jupiter-Sun-Orbit (JSO) coordinate system) of the Jovian magnetosphere boundary crossings is shown in Figure S1 in Supporting Information (SI). In the JSO system, X is aligned with the Jupiter-Sun vector, Y indicates the Sun’s motion in Jupiter frame, and Z closes the system.

149

150

151

152

153

154

155

156

157

158

159

160

In this study, the boundary crossings displayed Figure 1 were determined using the radio measurements of the low frequency receiver of the Juno/Waves instrument (Kurth et al., 2017), and the magnetic field measurements of the Juno/MAG instrument using the Fluxgate Magnetometer measurements (Connerney et al., 2017), following the work done by Hospodarsky et al. (2017). Three examples are shown in Figure 2, with Juno/Waves data (using C. K. Louis et al., 2021a, 2021b, estimated flux density data set) displayed in the top panels, and Juno/MAG data (in spherical JSO coordinates system) in the bottom panels. The “out” crossings (black dashed lines) correspond to a boundary moving towards Jupiter, e.g., Figure 2a,d, Juno crosses the bow shock going from the magnetosheath to the solar wind. The “in” crossings (grey shaded lines) define a boundary moving away from Jupiter, e.g., Juno crosses the bow shock, leaving the solar wind to enter the magnetosheath.

161

162

163

164

165

166

167

168

The bow shock is a discontinuity formed when the supersonic solar wind is slowed to subsonic by interaction with the Jovian magnetic obstacle. A bow shock crossing is detected from the change in magnetic field amplitude and in the level of field fluctuations in the Juno/MAG data between the solar wind and the magnetosheath (Figure 2d). In the Juno/Waves measurements (Figure 2a) one can observe (i) an intense and broadband signal at the crossing and (ii) Langmuir waves when Juno is inside the solar wind, visible here at ~ 10 kHz, which are produced by solar electrons reflected back into the solar wind from the shock boundary (Scarf et al., 1971; Filbert & Kellogg, 1979).

169

170

171

172

173

174

175

176

177

178

179

180

181

The position of the magnetopause is determined by the balance between the solar wind dynamic pressure and the plasma pressure in the outer magnetosphere (Mauk et al., 2004). A magnetopause crossing is detected by the appearance/disappearance in the Juno/Waves data (see Figure 2b) of the trapped continuum radiation, usually observed between 0.5 kHz and 2 kHz. This signal is only seen when the observer is inside Jupiter’s magnetosphere, in this example before the black-dashed line at $\sim 2017-06-18T09:00$, and after the grey-shaded line at $\sim 2017-06-19T03:00$. This trapped continuum radiation propagates at a frequency lower than the plasma frequency inside the magnetosheath and therefore can not propagate into the magnetosheath (hence the name “trapped”). Juno/MAG measurements of the magnetic field amplitude (Figure 2e) also show a change as Juno crosses the magnetopause, passing from the magnetosphere into the magnetosheath (see, e.g., black-dashed line at $\sim 2017-06-18T09:00$), with a decrease in magnetic field total amplitude $|B|$ and a much more disturbed signal than in the magnetosphere.

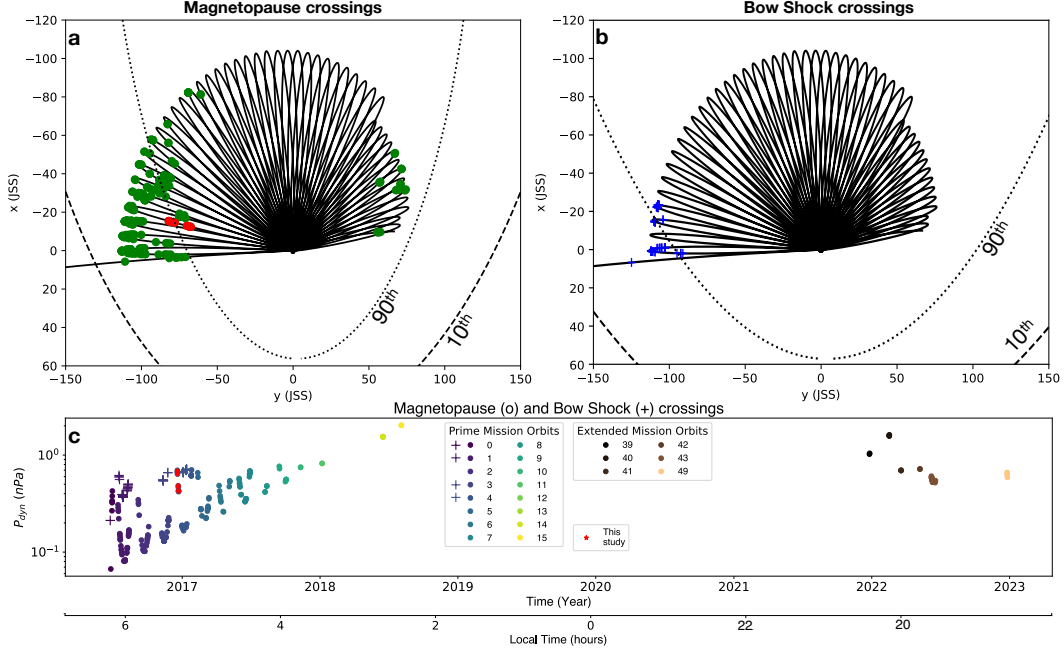


Figure 1. Projection of the Juno trajectory into the equatorial plane, with the (a) magnetopause and (b) bow-shock crossings overplotted. The magnetopause crossings studied in this article are highlighted in red in panel (a). The coordinate system used here is the Jupiter-de-Spun-Sun (JSS). In this system, X points towards the Sun, Z is aligned with the Jovian spin axis, and Y closes the right-handed system (positive towards dusk). In panel (a) the dashed line represents the 10th quantile position of the magnetopause (0.03 nPa), the dotted line its 90th quantile position (0.518 nPa). In panel (b) these same lines represent the 10th (0.063 nPa) and 90th (0.579 nPa) quantile positions of the bow shock (values from Joy et al., 2002). Panel (c) displays the solar wind dynamic pressure P_{dyn} values inferred from Joy et al. (2002), for each crossing (“+”: magnetopause; “o”: bow shock), as a function of time and Local Time (1200: direction of the Sun; 0000: opposition to the Sun). The colour code corresponds to the orbit number. The cases studied in this article are highlighted in red.

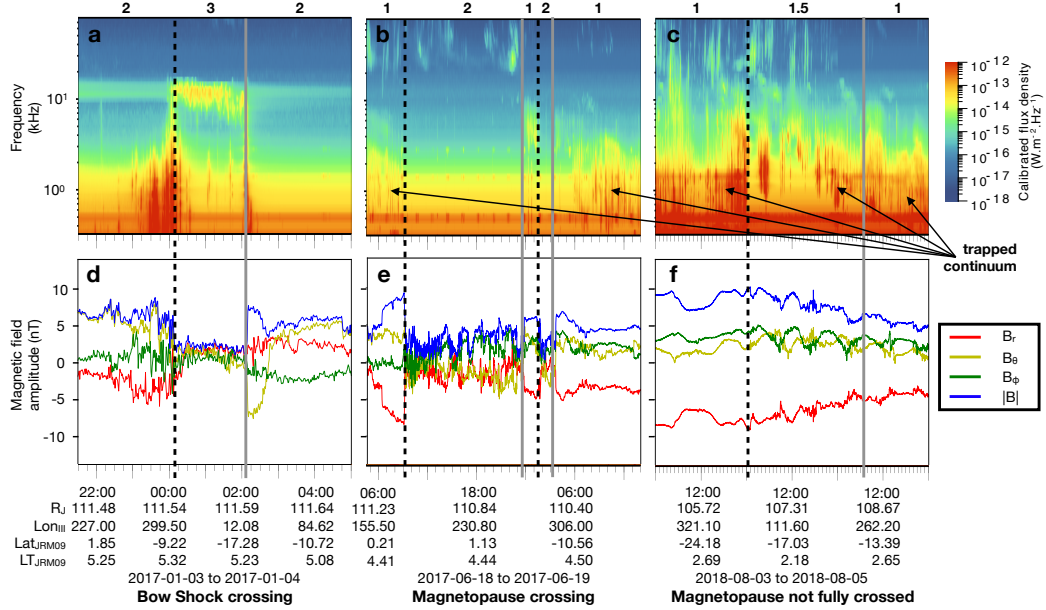


Figure 2. Examples of magnetospheric boundary crossings. Top panels (a-c) display Juno/Waves measurements (using C. K. Louis et al., 2021a, 2021b, estimated flux density data set), while bottom panels (d-f) display Juno/MAG measurements in spherical JSO coordinates. Outbound crossings (boundary moving towards Jupiter) are highlighted by the black-dashed lines, while inbound crossings (boundary moving away from Jupiter) are highlighted by the grey-shaded lines. (left (a,d)) Bow shock crossings; (middle (b,e)) Magnetopause crossings; (right (c,f)) Example where the Juno spacecraft partially crossed the magnetopause without ever actually passing from the magnetosphere to the magnetosheath (i.e. moved around the border). The numbers above the Waves data indicate the region where Juno is located: (1): Magnetosphere, (2) Magnetosheath, (3) Solar Wind, (1.5): “in” the magnetopause boundary.

182 In some observations (see Figure 2c, between black-dashed and grey-shaded lines),
 183 low and high cut-off frequencies of the trapped continuum increase. Before \sim 2018-08-
 184 04T00:00 (black-dashed line) and after \sim 2018-08-05T07:00 (grey-shaded line), the trapped-
 185 continuum radiation is visible between \sim 0.3 kHz and \sim 4 kHz. In-between, the trapped-
 186 continuum radiation is no longer visible at low frequency, but is shifted to higher frequen-
 187 cies (between \sim 0.6 and \sim 8 kHz) and is very bursty. The high frequency part never
 188 completely disappears, and no drastic change in magnetic field components (Figure 2f)
 189 is observed, although they are more disturbed than in the magnetosphere, but less than
 190 in the magnetosheath. In the observation shown in Figures 2c,f, Juno is on the outbound
 191 part of its trajectory and is therefore moving away from Jupiter. We interpret these ob-
 192 servations as the movement of the magnetopause towards Juno at first (increase of low
 193 and high cut-off frequencies, see black-dashed line). Subsequently, the magnetopause stops
 194 moving towards Jupiter, and Juno never completely crosses the magnetopause to end
 195 up in the magnetosheath (between black-dashed and grey-shaded lines). Juno is how-
 196 ever close enough to the magnetopause, or even in the boundary layer (Went et al., 2011),
 197 to observe an increase of the low-frequency cutoff of the trapped continuum by the in-
 198 creasing density when approaching the boundary. Finally, the magnetopause is moving
 199 away from Jupiter (faster than Juno’s velocity), and high and low cut-off frequencies de-
 200 crease (Juno is again completely in the magnetosphere).

201 From the boundary positions, we can infer the solar wind dynamic pressure P_{dyn}
 202 using the Joy et al. (2002) model, by solving their second order polynomial equation (equation
 203 1 of Joy et al., 2002). From this, we can determine if the crossings of the magnetospheric
 204 boundaries are due to compressions of the magnetosphere, by comparing the inferred P_{dyn}
 205 values to either Joy et al. (2002) quantile values, or observed solar wind P_{dyn} distribu-
 206 tions upstream of Jupiter (Jackman & Arridge, 2011). One should note that the P_{dyn}
 207 value determined using Juno’s position is not absolute, but a lower limit of the dynamic
 208 pressure. Although Juno is outbound, we cannot directly infer how far the magnetopause
 209 boundary is pushed back towards Jupiter.

210 Figure 1c displays the inferred P_{dyn} for all crossings (“+”: magnetopause; “o”: bow
 211 shock) as a function of time and Local Time. Note that there is a trend of increasing P_{dyn}
 212 values with time and decreasing Local Time. This is due to the procession of orbits, tak-
 213 ing Juno more and more towards the night side of the magnetosphere (midnight Local
 214 Time), and thus deep into the magnetotail. This means that the magnetosphere has to
 215 be more compressed for Juno to cross the magnetospheric boundaries from this location.
 216 The bow shock is even further out again and thus Juno did not encounter the dawn side
 217 bow shock after the first few Juno orbits.

218 In the absence of an upstream monitor, we can compare these inferred P_{dyn} val-
 219 ues with those provided by solar wind propagation models (e.g., Tao et al., 2005). For
 220 this, we must take into account any uncertainty on the propagation model values due
 221 to angle from opposition where predictions are most reliable. From this propagation model,
 222 we can also infer the type of shock (FFS or FRS) that compresses the magnetosphere
 223 as discussed in Section 1.

224 The full list of magnetopause and bow shock crossings (from 2016-06-24 to 2022-
 225 07-26, i.e. up to orbit 41) are available in Table S1 and S2 in Supplementary Informa-
 226 tion (SI), along with the position of Juno (in cartesian JSS –mandatory to use Joy et
 227 al. (2002) model– and cartesian and spherical International Astronomical Union (IAU)
 228 System III (SIII) coordinates system), the inferred solar wind dynamic pressure and the
 229 position of the magnetosphere standoff distances (bow shock and magnetopause) inferred
 230 from the Joy et al. (2002) model (C. K. Louis et al., 2022e). Figure S2 displays statis-
 231 tical distributions based on the magnetosphere boundary crossings (Local Time, Solar
 232 Wind dynamic pressure, magnetopause and bow shock positions).

233 We next investigate the response of bKOM and DAM emissions to magnetospheric
 234 compression in a case study. For that, we use the C. K. Louis et al. (2021a) dataset (C. K. Louis
 235 et al., 2021b) and catalogue of the radio emissions (C. K. Louis et al., 2021c). This cat-
 236 alogue contains the Jovian radio emissions identified in the Juno/Waves observations,
 237 only from 2016-04-09 to 2019-06-24 (e.g. up to the 21st apoJove of Juno). The radio com-
 238 ponents were visually identified according to their time-frequency morphology and then
 239 manually encircled by contours and labeled, using a dedicated program that records the
 240 coordinates of the contours and the label of each emission patch (C. Louis et al., 2022a;
 241 C. K. Louis et al., 2022b). While nKOM patches can be identified individually (fuzzy
 242 patches of emission elongated in time), the bKOM and DAM components have not been
 243 explicitly catalogued because they are the most frequent emissions in their respective fre-
 244 quency range. They can be selected and studied by excluding all other components and
 245 restricting to the adequate frequency range. For example, excluding nKOM in the range
 246 20-140 kHz allows one to select the bKOM component only. In the [3.5-40.5] MHz fre-
 247 quency range, only decametric emissions induced by the Galilean moons Io, Europa and
 248 Ganymede have been labelled (based on C. K. Louis, Hess, et al. (2019) simulations of
 249 those radio emissions, see C. K. Louis et al. (2020) for more details). Therefore, by ex-
 250 cluding them, only auroral DAM emissions remain in this range. Given that HOM emis-
 251 sions can extend up to a few MHz, the highest part of the hectometric emission could
 252 be present in this range, but would only represent a minority of the emissions observed.

253 For the case studies described in Section 3, we decided to select the magnetopause
 254 crossings that took place between 2016-12-19 and 2016-12-23, highlighted in red in Fig-
 255 ure 1. This choice is based on three factors: (i) in 2016-2017, the Jovian Auroral Dis-
 256 tributions Experiment (JADE, McComas et al., 2017) was not activated during excursions
 257 into the solar wind, excluding *in situ* plasma information, and thus a direct mea-
 258 surement of P_{dyn} . Therefore, we decided to choose among one of the (more numerous)
 259 magnetopause crossing cases; (ii) the case chosen had to be within the time interval cov-
 260 ered by the catalogue of C. K. Louis et al. (2021a, i.e. between 2016-04-09 and 2019-06-
 261 24); (iii) in order to avoid any bias related to an extremely exceptional case, we did not
 262 select the case with the highest P_{dyn} value (second half of 2018, orbit 15).

263 The time interval chosen presents two main advantages. (i) There are two sets of
 264 crossings in a row. The P_{dyn} value determined for the first crossing (2016-12-19T01:50)
 265 is 0.70 nPa. The dynamic pressure associated with the second set of crossings (2016-12-
 266 21T08:48) is 0.48 nPa. The distribution of P_{dyn} at Jupiter published by Jackman and
 267 Arridge (2011, see their Figure 4b) reveals a peak at 0.05 nPa and a maximum slightly
 268 above 1 nPa. The 0.48 and 0.70 values therefore lie towards the tail of this distribution.
 269 Moreover, these inferred values are close to the 90th quantile value (0.518 nPa) of the
 270 magnetopause position given by Joy et al. (2002). Therefore, these two sets of magne-
 271 topause crossings correspond to a strong and a moderate compression. (ii) Based on Fig-
 272 ure 1c (red points) the P_{dyn} values associated with these magnetopause crossings are well
 273 above the “trend”, and therefore correspond to the strongest compressions during or-
 274 bit 4. Recall that this “trend” is due to the procession of Juno’s orbit, taking the space-
 275 craft deep into the magnetotail, implying that the magnetosphere needs to be more com-
 276 pressed for Juno to cross the magnetospheric boundaries.

277 **3 Jovian auroral radio emission response to compressions of the mag-** 278 **netosphere**

279 **3.1 Determination of the compression**

280 Figure 3 displays Juno measurements during magnetopause crossings for a 7-day
 281 interval from 2016-12-17T00:00 to 2016-12-24T04:15. Black-dashed lines show when Juno
 282 crossed the magnetopause from the magnetosphere to the magnetosheath (outbound cross-
 283 ings), while grey-shaded lines show inbound crossings. Figures 3a,b display Juno/Waves

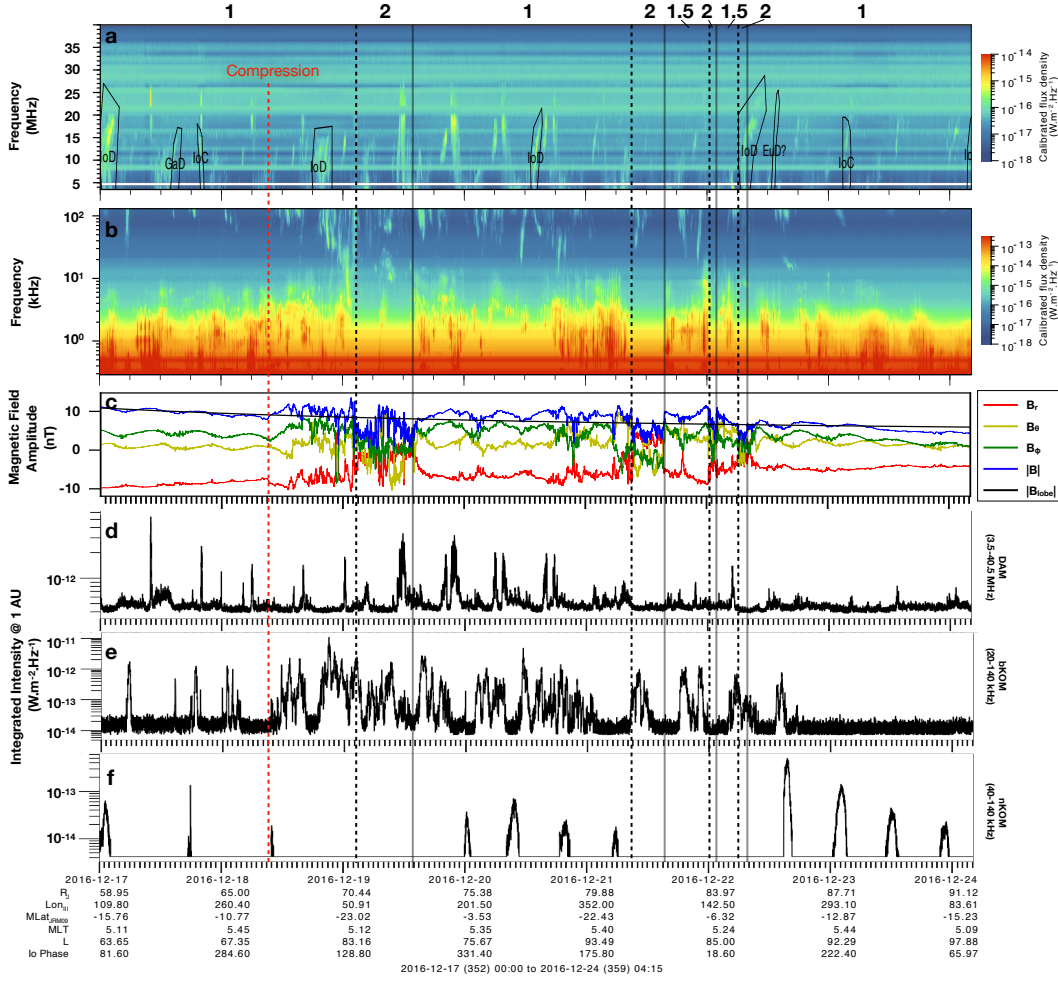


Figure 3. (a-c) Juno Waves and MAG measurements during a series of magnetopause crossings. Panels (a) and (b) show Juno Waves frequency-time spectrograms covering two different frequency ranges (from 3.5 to 40.5 MHz and between 3 kHz and 140 kHz, respectively), with the black polygons in the top panel denoting the radio emissions induced by the interaction between Jupiter and its moons (e.g. Io, Europa or Ganymede, based on C. K. Louis et al., 2021c). Panel (c) shows the three components of magnetic field (in JSO spherical coordinates system, red, yellow and green lines) and total field strength (blue). The black line displays the Kivelson and Khurana (2002); Khurana et al. (2004) magnetic field variation fit. Panels (d-f) display time series of integrated flux density (normalized at 1 Astronomical Unit (AU), 15 sec time resolution) for (d) the auroral decametric (DAM, in the 3.5-40.5 MHz range) not induced by the interaction between Jupiter and its moons (i.e. all the non-labelled emissions), (e) broadband kilometric (bKOM, in the 20-140 kHz range) and (f) narrowband kilometric (nKOM, in the 40-140 kHz range) radio emissions.

The black-dashed lines represent the outbound magnetopause crossings (from the magnetosphere to the magnetosheath) while the grey-shaded lines represent the inbound magnetopause crossings (from the magnetosheath to the magnetosphere). The red-dashed line represents the time when Juno starts to measure magnetic fluctuations and $|B| > |B_{lobe}|$ (panel c), and an increase in the low and high cut-off frequencies of the trapped-continuum radiation (panel b).

The numbers above the Waves data indicate the region where Juno is located: (1): Magnetosphere, (2) Magnetosheath, (1.5): “in” the magnetopause boundary.

284 measurements for two different frequency ranges: (a) [3–40.5] MHz and (b) [0.3–140.0] kHz.
 285 Figure 3c displays Juno/MAG measurements: total amplitude $|B|$, and (r, θ, ϕ) compo-
 286 nents in JSO spherical coordinates system. The black line displays the Kivelson and Khu-
 287 rana (2002); Khurana et al. (2004) magnetic field variation fit in the lobes (beyond $r =$
 288 30 Jovian radii, the lobe magnetic field falls off as $B_{\text{lobe}}(\text{nT}) = (2.94 \pm 0.07) \times 10^3 r^{-1.37 \pm 0.01}$).
 289 Therefore, for an observer inside the magnetosphere, and if the magnetosphere is in a
 290 steady-state, $|B|$ should follow $|B_{\text{lobe}}|$. Figures 3d,e,f display integrated time series of the
 291 radio signal measured by Juno/Waves for three different radio components: (d) auro-
 292 ral DAM (i.e. excluding the satellite-related DAM emissions), (e) bKOM, and (f) nKOM.

293 As described in Section 2 (see Figures 2b,e), the magnetopause crossings are clearly
 294 seen in Figure 3b from the disappearing of the trapped continuum radiation and in Fig-
 295 ure 3c from the change in the magnetic field components and total amplitude (see the
 296 black-dashed and grey-shaded lines). Looking in more detail at Juno/MAG measurements
 297 (Figure 3c), one can notice at $\sim 2016-12-18\text{T}09:00$ (indicated by the red dotted line),
 298 i.e., ~ 18 h before the crossing of the magnetopause, an increase of the $|B|$ (blue curve)
 299 and B_ϕ (green curve) components while the B_r (red curve) and B_θ (yellow curve) com-
 300 ponents decrease. This is followed by turbulence observed in all magnetic field compo-
 301 nents, but without the sharp decrease in $|B|$ characteristic of magnetic measurements
 302 in the magnetosheath. We also see, approximately at the same time, that the cut-off fre-
 303 quencies of the trapped continuum are increasing (Figure 3b): the trapped continuum
 304 is observable in the $[\sim 0.4-3]$ kHz frequency range before the red-dashed line, and in the
 305 $[\sim 0.8-5]$ kHz frequency range between the red-dashed and black-dashed lines. This change
 306 in the cut-off frequencies is due to the inward motion of the magnetopause during the
 307 compression. Because of this, the local density along Juno’s path is increasing, and there-
 308 fore the low-frequency part of the trapped continuum cannot propagate, resulting in an
 309 increase in the cut-off frequencies of the trapped continuum. All these characteristics are
 310 the signature of the inward motion of the magnetopause boundary towards the space-
 311 craft (see Figures 2c,f).

312 Furthermore, comparing the total amplitude of the magnetic field $|B|$ (blue curve)
 313 to Kivelson and Khurana (2002); Khurana et al. (2004) magnetic field variation fit $|B_{\text{lobe}}|$,
 314 one can see that before $\sim 2016-12-18\text{T}09:00$ (red dotted line), $|B|$ and $|B_{\text{lobe}}|$ follow the
 315 same trend. However, between $\sim 2016-12-18\text{T}09:00$ and the crossing of the magnetopause
 316 (first black dashed-line), $|B|$ is above $|B_{\text{lobe}}|$, which is a clear sign that the magnetosphere
 317 is being compressed (see e.g., Jackman et al., 2010).

318 All these elements lead us to interpret this as representative of the beginning of the
 319 impact of a stronger solar wind on the magnetosphere, and thus the beginning of com-
 320 pression. On the other hand, after Juno crosses the magnetopause for the second time
 321 (back into the magnetosphere, grey-shaded line) on $\sim 2016-12-19\text{T}14:12$ and until the
 322 next outward crossing of the magnetopause ($\sim 2016-12-21\text{T}08:48$), we observe the same
 323 features: a variable low and high cut-off frequencies of the trapped continuum, small per-
 324 turbations in the magnetic field components, and $|B| > |B_{\text{lobe}}|$. We interpret this as
 325 the relaxation phase of the magnetosphere, but not to a fully extended state. From the
 326 observations, we can deduce that Juno remains very close to the magnetopause (same
 327 characteristics as in Figures 2c,f), before the second compression takes place and the space-
 328 craft is again in the magnetosheath.

329 By comparing the time spent by Juno inside the magnetosheath during the two com-
 330 pression events, we can infer whether one of the compressions was stronger than the other,
 331 i.e., lasted longer or the magnetopause was pushed further inwards. During the first pass
 332 from the magnetosphere to the magnetosheath, Juno stayed in it for ~ 12 h 20 min, whereas
 333 during the second pass, Juno stayed inside the magnetosheath less than 7 h, before go-
 334 ing back into the magnetosphere very quickly twice for a few minutes. Therefore, we can
 335 deduce that the first compression either lasted longer or the magnetopause was pushed

336 further inwards. In any case, we can infer that the magnetosphere was probably more
337 disturbed by the first compression.

338 The Tao et al. (2005) solar wind propagation model is more reliable when Earth
339 and Jupiter are in conjunction as seen from the Sun (Jupiter-Sun-Earth angle equal to
340 0°). During the time range displayed in Figure 3, the Jupiter-Sun-Earth angle is -110°
341 (in average). Therefore, the error in timing on Tao et al. (2005) solar wind propagation
342 model can be as large as 2 days or more, the time interval between the shocks can also
343 be shifted, and P_{dyn} can be misjudged. Therefore, the outputs from the Tao et al. (2005)
344 model should be used here only as a guide. For that reason, they are only displayed in
345 the SI (Figure S3-S4), for information. According to Tao et al. (2005) model, two shocks
346 arrive at Jupiter successively in a time interval of two and a half days. The model pre-
347 dictes the arrival of the first compression at the beginning of day 2016-12-16, i.e. two days
348 before the first compression observed by Juno. By shifting the model outputs by two days
349 (see Figure S4), we obtain a good match between the arrival of the two shocks at Jupiter
350 and the compressions observed by Juno. These two shocks have very different charac-
351 teristics (see Figure S3): (i) the first one shows an increase in the solar wind speed and
352 a sharp decrease in the solar wind density and temperature, while (ii) the second shock
353 shows an increase in the solar wind speed, density and temperature. Thus, if we take the
354 outputs of Tao et al. (2005) model as reliable, the first shock would be a Fast Reverse
355 Shock (FRS) while the second would be a Fast Forward Shock (FFS).

356 **3.2 Response of the auroral radio emission to the first compression**

357 Having determined the start time of the compression and the associated dynamic
358 pressure, let us now study the response of the radio emissions to the first compression.

359 **3.2.1 Broadband kilometric (bKOM) emission**

360 The bKOM emissions (Figure 3e) are the first to show a strong variation. Before
361 the onset of the compression, we can see some peaks in the integrated intensity, but re-
362 stricted to a narrow frequency range (few 10s of kHz, see Figure 3b). Immediately af-
363 ter (dashed-red line at $\sim 2016-12-18\text{T}09:00$), we observe emissions almost continuously,
364 with an increase in the integrated intensity. This increase can be explained by both the
365 observations of bKOM emissions over a much wider frequency range, i.e. from 20 kHz
366 to 140 kHz (see Figure 3b), and by the increase intensity of the emission. Very low fre-
367 quency extensions of the emission, i.e., emissions extended down to 20 kHz, are only vis-
368 ible over ~ 1 h 15 min, thus only for specific sources. The bKOM emissions seen at al-
369 most every longitude are then observed until $\sim 2016-12-21\text{T}02:00$, thus over more than
370 60 hours. The observation of emissions on an almost continuous basis tells us that sources
371 have been activated at almost all longitudes. It should be noted that no bKOM emis-
372 sions seem to be observed between 2016-12-18T17:00 and 19:00. A sector of longitude
373 therefore seems to have no associated bKOM emissions, at least during the first rota-
374 tion. This could be due to various reasons, such as emissions that are too weak to be de-
375 tected, geometric effects preventing the emission from being beamed towards the observer,
376 or a sector that is completely non-activated.

377 **3.2.2 Decametric (DAM) emission**

378 After compression, an increase in the integrated intensity of the DAM radio emis-
379 sions is also observed. However, unlike the bKOM emissions, this is not observed simul-
380 taneously with the onset of the magnetic disturbances, nor is it continuous over time.
381 DAM emissions visible before the compression (non-labelled vertex early arc up to 15
382 MHz, see Figure 3a, statistically reported by Imai et al., 2017) are still visible during the
383 compression with the same rotation period, however their intensity has increased com-
384 pared to before the compression. Therefore, the appearance of these emissions is prob-

ably modulated by rotation and independent of any compression. However, compression seems to have an impact on their intensity. New emissions, more intense and extending up to 25-30 MHz, appear at $\sim 2016-12-19T12:00$, i.e. ~ 28 hours after the compression, and last for ~ 30 hours. Their rotation period is longer than the previously visible DAM emissions, visible with the double peak in the integrated time series Figure 3d, which means that the sources are sub-corotating (see below).

Since the CMI emissions are not isotropically emitted, but only emitted at the edge of a hollow cone, with an angle of $\sim 75^\circ$ to $\sim 90^\circ$ with respect to the local magnetic field line (see Section 1), geometry effects are important, and emission is mostly seen by an observer when the sources are at a longitude $\sim 75^\circ$ to 90° greater or lower than the longitude of the observer. It can thus be complicated to disentangle between “no emission” and “non-visible emission”, because the observer is not in the beam of the emission. For this, it can be interesting to have multi-point observations, e.g., including ground-based radio telescopes such as the Nançay Decameter Array (NDA). Figures 4 displays observations taken by Juno (4a) and NDA (4b) on 2016-12-19. The observation geometry is shown in Figure 4c, with Juno located at a mean local time of 5.2 hours, and NDA at a mean local time of 12.64 hours, at the moment of the observations of the radio emissions. Finally, Figure 4d shows the shape of the radio emission as a function of the position of the sources relative to the observer.

Multiple “B” arcs are observed by Juno up to almost 30 MHz, between 11:00 and 12:30 (Figure 4a, see also Imai et al., 2017, who statistically reported these arcs). The type of the arcs and the position of Juno indicates that the emissions come from the midnight-to-dusk side as seen from Juno (see Figures 4c,d). On the other hand, between 09:00 and 09:30, “A” emissions are observed by the NDA (Figure 4b) up to almost 30 MHz. The type of the emissions seen by the NDA, and its position relative to Jupiter, indicates the emissions come from the dusk side as seen from Earth (see Figures 4c,d). By studying the time delay (e.g., at 24.5 MHz) between the first emission seen on 2016-12-19T09:08 by the NDA (Earth Time, i.e. $\sim 2016-12-19T08:23$ Juno Time, taking into account the light travel time) and the first emission seen on 2016-12-19T12:27 (Juno Time) by Juno, we obtain a $\delta t = 4.1$ h. According to the local time positions of the two observers, this is consistent with an emission originating from the same source, seen from both side of the beaming cone, and rotating with a sub-corotation rate of 70 ± 5 %, meaning that the source is rotating at 70 % of Jupiter’s rotation angular frequency (taking into account that the emission at 24.5 MHz is beamed along a hollow cone with aperture angle of $75^\circ \pm 5^\circ$, C. K. Louis et al., 2017).

The beaming angle allowed by the CMI is in the range 75° – 90° , and Juno does not see a “B” radio emission before the NDA. Therefore the onset region must be located in a region greater than Junos local time plus 75° – 90° , and lower than NDAs local time minus 75° – 90° , therefore in the local time range $[1110-1740] \pm 0100$ hours.

The lack of emission observed by Juno is therefore partly due to geometry effects, but probably also to a delay in the activation of the sources and in a specific region (dusk). Indeed, the NDA sees an emission before Juno, but no emission is seen by Juno at the previous rotation, indicating that a time delay exists between the compression of the magnetosphere and the activation of newly activated DAM sources. This exact time delay is difficult to determine here, and would require a more statistical study or more observers, but it seems that at least two Jovian rotations are needed before new DAM sources are activated.

3.2.3 *Narrowband kilometric (nKOM) emission*

Finally, the delay for new nKOM emissions to be visible is far longer than for bKOM and DAM emissions. The first new emission appears at $\sim 2016-12-20T00:00$, i.e. 39 hours after the first visible bKOM emission. The interval between the peaks in the integrated

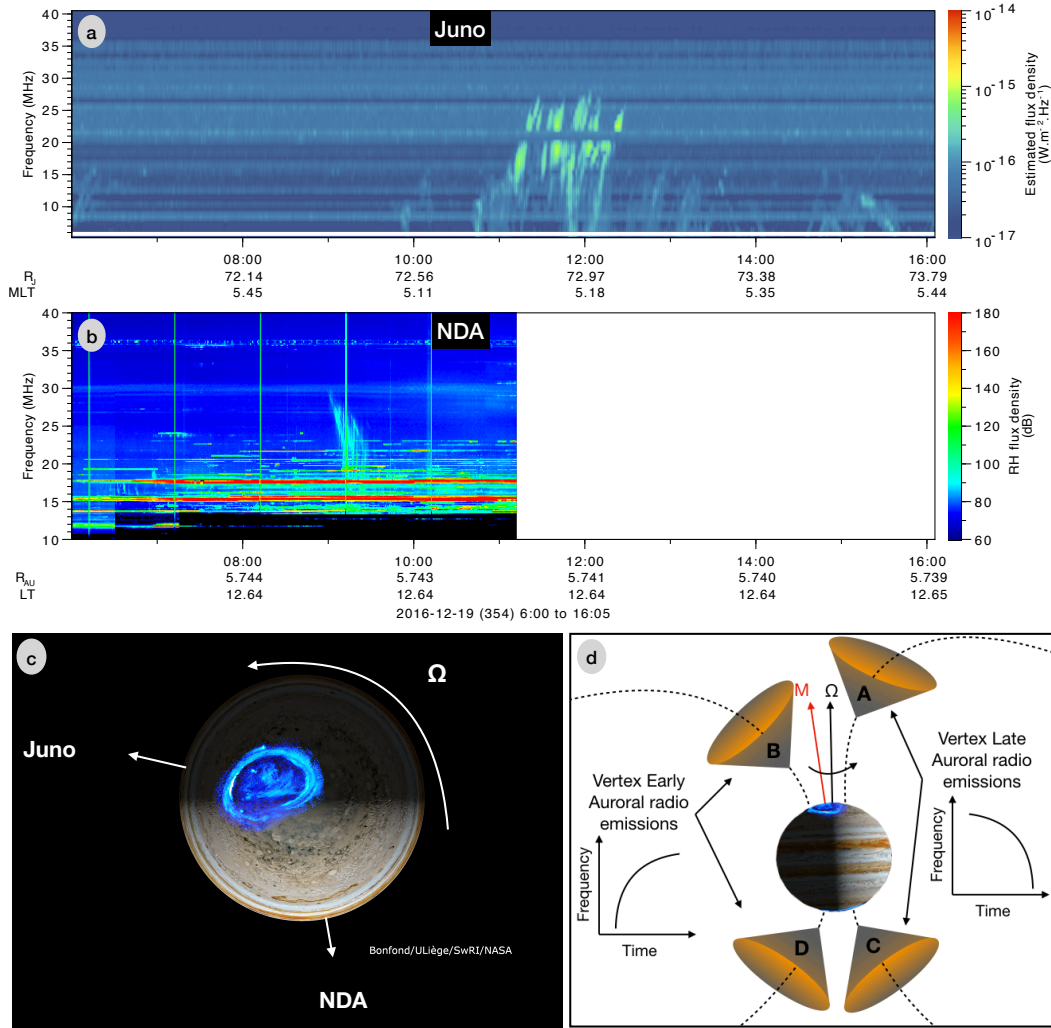


Figure 4. (a) Juno Waves and (b) Nançay Decameter Array (NDA) routine receiver observations. Decametric radio emissions are clearly visible (a) between 11:00 and 12:30 (Spacecraft Event Time) and (b) between 09:00 and 09:30 (UT time). The light travel time between Juno and Earth is ~ 47 minutes. The data gap after 11:10 is due to the fact that Jupiter is no longer visible in the sky from the NDA observatory. (c) Observers' configuration. (d) Cartoon of the geometry and nomenclature of the auroral radio emissions and corresponding arc-shape in the (time, frequency) plane. If the source is located to the West of Jupiter for the observer (sources “B” or “D”), the emission will have a vertex early arc shape. If on the contrary the source is located to the East of Jupiter for the observer (sources “A” or “C”), the emission will have the shape of a vertex late arc.

The arcs observed in panels (a) and (b) originate from the same source. NDA sees the emission cone exiting its field of view (vertex late arc) while Juno sees the emission cone entering its field of view (hence vertex early arc).

436 intensity is not regular, and varies between ~ 9 h 14 min, ~ 10 h 22 min and ~ 9 h 44 min.
 437 A closer look to the intensity peaks at different frequencies (see Figure S5b) shows that
 438 the signal at lower frequencies (e.g., from 70.862 kHz to 112.43 kHz) is triggered before
 439 the signal at higher frequencies (e.g., at 126.16 kHz and 141.54 kHz), and then disap-
 440 pears first. The interval between the peaks seems to be different depending on the fre-
 441 quency, which implies different source locations (see Section 3.3, and Section 4, for more
 442 details).

443 3.3 Response of the auroral radio emission to the second compression

444 As mentioned at the beginning of this section, the dynamic pressure of the solar
 445 wind during the second compression event is potentially weaker than during the first event.
 446 This is suggested by both (i) the position of the magnetopause, further away from Jupiter
 447 (see the second dotted black line at 2016-12-21T08:48), and (ii) the time spent in the
 448 magnetosphere which is shorter than during the first event.

449 The inspection of the radio emission time series shows that one DAM emission is
 450 observed at $\sim 2016-12-21T21:30$, also observed one rotation later with greater inten-
 451 sity. This emission is most likely the reactivation of previously observed sources (as ob-
 452 served during the first compression event). Indeed DAM emission with decreasing inten-
 453 sity is observed ~ 20 hours before ($\sim 2016-12-21T01:30$) with the same shape. Since
 454 the NDA is observing only one third of the time we have no contemporaneous observa-
 455 tions for this event.

456 New bKOM emission sources are activated at $\sim 2016-12-21T08:00$. However, in
 457 contrast to the first event, fewer bKOM sources seem to have been activated, since the
 458 bKOM emission is not visible at all times, and the sources are activated for a shorter pe-
 459 riod of time (only visible for ~ 30 hours vs. ~ 60 hours).

460 Finally, regarding the nKOM emission, new nKOM emissions are activated, start-
 461 ing at $\sim 2016-12-22T15:00$, and lasting for ~ 40 hours (same duration as for the first
 462 compression), with integrated intensity higher than for the first event. This time, the
 463 delay between the activation of the bKOM and the nKOM emissions is only ~ 31 hours.
 464 Again, it can be seen that the period between the peaks in the integrated intensity is not
 465 regular. It varies between ~ 10 h 30 min, ~ 9 h 50 min and ~ 10 h 54 min. A closer
 466 look to the intensity peaks at different frequencies (see Figure S5c) shows that the sig-
 467 nal is first triggered at the lowest frequencies before being triggered at the highest fre-
 468 quencies. Then the signal disappears, or fades, in the same order. The interval between
 469 two peaks is different depending on the frequency. Focusing on distribution peaks at each
 470 frequency, it can be seen that periodicity increases with decreasing frequency. When the
 471 new nKOM emissions are activated, all peaks are almost centered at the same time (\sim
 472 $2016-12-22T15:45$); one rotation later, the peaks are distributed in order of decreasing
 473 frequency, with the 141.54 kHz signal seen first and the 89.172 kHz signal peak seen last.
 474 This could be explained by the fact that the lower frequency nKOM is generated at lower
 475 density, hence, larger radial distances from Jupiter: the deviation from rigid co-rotation
 476 would be greater farther from the planet, and the periodicity should be longer.

477 4 Summary, Discussion and Perspectives

478 In this paper, we have presented in Section 2 a set of magnetospheric boundary cross-
 479 ings (See Figure 1). More detailed information on each crossing, such as their exact time,
 480 their positions in different coordinate systems, and several added values (P_{dyn} , magne-
 481 topause and bow shock standoff distances) are given in Supporting Information (Tables
 482 S1, S2), as well as statistical distributions for these added values (Figure S2). The files
 483 corresponding to Tables S1, S2 are accessible through C. K. Louis et al. (2022e).

Table 1. Table summarising the results of the study of the response time of radio emissions to compression, as seen by Juno. For each compression, the dynamic pressure of the solar wind (determined from the model of Joy et al., 2002), the type of shock (determined from the model of Tao et al., 2005), the response time of each component of the radio emission (main band of the bKOM, low frequency extension (LFE) of the bKOM, DAM and nKOM) and the activation time (as seen by Juno) are given.

Compression	P_{dyn} Joy et al. (2002)	Type of shock Tao et al. (2005)	Auroral radio emission	Activation time	Duration
1st compression	0.70	FRS	bKOM Main band LFE DAM nKOM	≤ 10 s min ~ 34 hours ~ 28 hours ~ 39 hours	~ 60 hours 1 h 15 min ~ 30 hours ~ 40 hours
2nd compression	0.48	FFS	bKOM Main band LFE DAM nKOM	≤ 10 min ≤ 10 min ~ 12 h 45 min ~ 31 hours	~ 30 hours ~ 15 hours 10 hours ~ 40 hours

484 In Section 3, we presented case studies of the response of Jovian radio emission to
 485 strong to moderate magnetospheric compressions, inferred by magnetopause crossings.
 486 Using the Joy et al. (2002) model, we calculated the dynamic pressure (lower limit) of
 487 the solar wind (see Table 1), and its main characteristics and type of shocks associated
 488 with these events using the Tao et al. (2005). We determined that the first magnetopause
 489 crossing is potentially due to (i) either a stronger and shorter compression, (ii) or higher
 490 solar wind dynamic pressure, based on the time spent by Juno in the magnetosheath.

491 We chose to study the magnetopause crossings occurring between 2016-12-17T00:00
 492 and 2016-12-24T04:15 (fourth orbit of Juno). These magnetopause crossings are among
 493 the innermost cases (see Figure 1a and S1a), corresponding to strong compressions ($P_{\text{dyn}} \subset$
 494 $[0.5-0.7]$ according to the Joy et al. (2002) model). These compressions occur when Juno
 495 is still on the dawn side of the magnetosphere, i.e. in a region where the model of Joy
 496 et al. (2002) is valid, in contrast to the dusk side where it is less constrained. Moreover,
 497 during this 7-day interval, we observe several magnetopause crossings, which can be grouped
 498 into 2 phases of magnetospheric compression. These two cases also seem to correspond
 499 to two different types of shock: FFS and FRS, according to the propagation model of
 500 Tao et al. (2005), with different responses observed in the radio components (see Table
 501 1).

502 Concerning the radio emission response to the compressions, we have determined
 503 that the bKOM sources are the first to be triggered, at almost every longitude, almost
 504 immediately after the observation of the first magnetic disturbances and density pertur-
 505 bations. The bKOM emission is then observed over 60 hours for the first compression
 506 and for 30 hours for the second one. Low Frequency Extensions, i.e. emissions going down
 507 to 20 kHz, are observed in both cases for a shorter duration.

508 In both cases, the DAM emissions are the second ones to be observed, at least one
 509 rotation after the start of the compression, and only in the noon-dusk sector, i.e. inside
 510 the local time range $[1110-1740]$. This sector includes that determined by Hess et al. (2012,
 511 2014), but is necessarily less precise given that we are only studying two cases here. A
 512 statistical study with Juno will provide further constraints, given the evolution of Juno's
 513 local time position during its mission. Our results seem to show that both FRS and FFS
 514 activate new, or re-activate, DAM emissions on the dusk side only. This is partially in
 515 agreement with Hess et al. (2012, 2014), who showed that FFS mainly trigger DAM emis-

516 sion on the dusk side, while FRS trigger emissions on the dusk and dawn sides. How-
 517 ever, since we are measuring radio emission only above 3.5 MHz in this study (due to
 518 Waves sensitivity) we are missing part of the DAM and most of the HOM emissions, that
 519 can go down to 0.3 MHz, while Hess et al. (2012, 2014) used Cassini radio measurements,
 520 down to 0.1 MHz. The DAM emission lasts for 30 hours in the first case, and 10 hours
 521 in the second case. In both cases, sources rotate in subcorotation, with a rate of $70 \pm$
 522 5% of rigid corotation. This value is comparable with the values obtained by Hess et
 523 al. (2012, 2014).

524 Concerning the activated nKOM emissions, we observe a strong difference compared
 525 to the bKOM and DAM emissions, with a long delay between compression and activa-
 526 tion of the nKOM sources (~ 30 to 40 hours). nKOM emission is then observed for \sim
 527 40 hours in both compression events. The periodicity of the nKOM peaks is frequency-
 528 dependent and increases with decreasing frequency. This would be related to the mech-
 529 anism, producing emissions at the plasma frequency which is proportional to the local
 530 plasma density. Therefore, low-frequency emissions are produced farther from Jupiter
 531 than higher-frequency emissions. The activation of new nKOM sources seems related to
 532 the relaxation/reconfiguration phase of the magnetosphere. As these emissions are pro-
 533 duced by different mechanisms, it is not surprising that the activation of these emissions
 534 is also different. However, it is possible that the energetic events observed by Louarn et
 535 al. (1998, 2016) could be caused or amplified by an expansion of the magnetosphere,
 536 which would amplify the centrifugal ejection of matter. It will therefore be mandatory
 537 to study in detail the nKOM during plasmashet distortion, which will require a list of
 538 magnetic disturbances measured during plasma sheet crossings, simultaneously to com-
 539 pression events. But this is beyond the scope of this current article, and will be the sub-
 540 ject of an upcoming study.

541 To get a better estimate of the conditions in the solar wind, such as the solar wind
 542 dynamic pressure and velocity, the Thomsen et al. (2019) analytical method could be
 543 used, based on Juno/JADE measurements inside the magnetosheath (Juno/JADE data
 544 were not available for the event studied in Section 3). This will be compared to estima-
 545 tion of the dynamic pressure obtained from Joy et al. (2002) magnetosphere boundaries
 546 model and Tao et al. (2005) propagation tool model. We could also use different solar
 547 wind propagation tools, such as “HuXT” model (Heliospheric Upwind Extrapolation with
 548 time dependence Owens et al., 2020), “WSA-ENLIL solar wind simulation”, “HelioCast”
 549 (Réville et al., 2023) or the “CDPP/Propagation Tool” extended to Jupiter (Rouillard
 550 et al., 2017).

551 To go further on the generalization of the response of Jovian radio emissions, the
 552 activation of new sources or the amplification of existing radio emissions, and their in-
 553 tensity to magnetospheric compression and solar wind characteristics (dynamic pressure,
 554 velocity, temperature, magnetic field orientation), a statistical study will be necessary.
 555 The same method will be used and will be applied to all the compression events deter-
 556 mined from the list of magnetopause crossings provided in the SI tables (see also Fig-
 557 ures 1 and SI1). This will involve using boundary crossings to infer compressions, ex-
 558 amining the response of associated radio emissions, and grouping case studies by prop-
 559 erties such as solar wind dynamic pressure, or shock type.

560 There are several benefits to a future statistical study. The first is to explore the
 561 differences between dawn and dusk side responses, and the different properties of the bound-
 562 aries of the magnetosphere (e.g., Kelvin-Helmholtz instability, Michael et al., 2021), or
 563 the differences in the observation of radio sources (beaming constraints). The second as-
 564 pect is the opportunity to explore different classes of behaviour in terms of magnetospheric
 565 compression state. Due to the precession of the apojoves, we observe the compression
 566 of the magnetosphere from different positions in the magnetosphere. As shown in Fig-
 567 ure 1c, the nature of the boundary motion is highly variable, and the number of bound-
 568 ary crossings varies greatly from one orbit to another. Some orbits have clean bound-

569 any crossings, while other orbits have multiple crossings in a short time. This makes it
 570 possible to study the radio response during the compression and relaxation phases, but
 571 also during the stationary state - see Figures 2c,f for an example. Thirdly, the long pe-
 572 riod of time between Juno's insertion into Jovian orbit (July 2016) and the latest orbits
 573 of the extended mission (perijoves ≥ 50) covers two different phases of two different so-
 574 lar cycle and different Jovian seasons, which could allow us to explore the response of
 575 radio emissions to compression as a function of the solar cycles and Jovian seasons.

576 At the time of writing, Juno is still crossing the boundaries on the high southern
 577 latitude dusk side, and thus a full statistical exploration of the broad parameter space
 578 should await the completion of these apojove passes. Moreover, the comprehensive la-
 579 belled radio emissions catalogue (C. K. Louis et al., 2021c) is currently being updated
 580 to cover the whole mission.

581 Acknowledgments

582 C. K. Louis', C. M. Jackman's, A. R. Fogg's and S. C. McEntee's work at the Dublin
 583 Institute for Advanced Studies was funded by the Science Foundation Ireland Grant 18/FRL/6199.
 584 The research at the University of Iowa is supported by NASA through Contract 699041X
 585 with Southwest Research Institute. D. M. Weights work at the Dublin Institute for Ad-
 586 vanced Studies was funded by European Unions Horizon 2020 research and innovation
 587 programme under Grant agreement No. 952439 and project number AO 2-1927/22/NL/GLC/ov
 588 as part of the ESA OSIP Nanosats for Spaceweather Campaign D. M. Weigt's work at
 589 Aalto University was funded from the European Research Council (ERC) under the Eu-
 590 ropean Unions Horizon 2020 research and innovation programme (project "SYCOS", grant
 591 agreement n^o 101101005). The research at the University of Iowa is supported by NASA
 592 through Contract 699041X with the Southwest Research Institute. WSK acknowledges
 593 the use of the Space Physics Data Repository at the University of Iowa supported by the
 594 Roy J. Carver Charitable Trust.

595 Data Availability Statements

596 The Juno/Waves dataset displayed in this paper, produced by C. K. Louis et al.
 597 (2021a), is accessible at <https://doi.org/10.25935/6jg4-mk86> (C. K. Louis et al., 2021b),
 598 and the catalogue can be download at <https://doi.org/10.25935/nhb2-wy29> (C. K. Louis
 599 et al., 2021c) . The Juno/MAG magnetic field data are accessible through the NASA/PDS
 600 website (Connerney, 2017). Figure 1 was produced using the Jupiter magnetosphere bound-
 601 aries crossings given in the SI Tables S1 and S2 (C. K. Louis et al., 2022e). Juno/Waves
 602 and Juno/MAG data were displayed using the Autoplot tool (Faden et al., 2010). The
 603 Nançay Decameter Array dataset displayed in Figure 4 is accessible at [https://doi.org/](https://doi.org/10.25935/PBPE-BF82)
 604 [10.25935/PBPE-BF82](https://doi.org/10.25935/PBPE-BF82) (Lamy et al., 2021). The routine that allows to determine the dy-
 605 namic pressure from the Joy et al. (2002) model are accessible at [https://github.com/](https://github.com/DIASPlanetary/jupiter_magnetosphere_boundaries)
 606 [DIASPlanetary/jupiter_magnetosphere_boundaries](https://github.com/DIASPlanetary/jupiter_magnetosphere_boundaries). Juno ephemeris and MAG data
 607 (in JSO coordinates system) were retrieved from <http://amda.cdpp.eu/> (Génot et al.,
 608 2021). Juno ephemeris used to infered the dynamic pressure (in JSS coordinate) were
 609 retrieved from <https://wgc.jpl.nasa.gov:8443/webgeocalc/#StateVector>.

610 References

- 611 Barbosa, D. D. (1982, May). Low-level VLF and LR radio emissions observed at
 612 earth and Jupiter. *Reviews of Geophysics and Space Physics*, *20*, 316-334. doi:
 613 10.1029/RG020i002p00316
- 614 Cecconi, B., Witasse, O., Jackman, C. M., Sánchez-Cano, B., & Mays, M. L. (2022,
 615 May). Effect of an Interplanetary Coronal Mass Ejection on Saturn's Ra-
 616 dio Emission. *Frontiers in Astronomy and Space Sciences*, *9*, 800279. doi:

- 617 10.3389/fspas.2022.800279
- 618 Collier, M. R., Gruesbeck, J. R., Connerney, J. E. P., Joy, S. P., Hospodarsky, G. B.,
619 Roberts, A., . . . Roelof, E. C. (2020, September). A K-Means Clustering
620 Analysis of the Jovian and Terrestrial Magnetopauses: A Technique to Classify
621 Global Magnetospheric Behavior. *Journal of Geophysical Research (Planets)*,
622 *125*(9), e06366. doi: 10.1029/2019JE006366
- 623 Connerney, J. E. P. (2017). *Juno MAG CALIBRATED DATA V1.0, JNO-J-3-*
624 *FGM-CAL-V1.0 [dataset]*. doi: 10.17189/1519711
- 625 Connerney, J. E. P., Benn, M., Bjarno, J. B., Denver, T., Espley, J., Jorgensen,
626 J. L., . . . Smith, E. J. (2017, November). The Juno Magnetic Field Investiga-
627 tion. *Space Science Reviews*, *213*, 39-138. doi: 10.1007/s11214-017-0334-z
- 628 Echer, E., Zarka, P., Gonzalez, W. D., Morioka, A., & Denis, L. (2010, Septem-
629 ber). Solar wind effects on Jupiter non-Io DAM emissions during Ulysses
630 distant encounter (2003-2004). *Astronomy & Astrophysics*, *519*, A84. doi:
631 10.1051/0004-6361/200913305
- 632 Faden, J. B., Weigel, R. S., Merka, J., & W., F. R. H. (2010, June). Autoplot: a
633 browser for scientific data on the web. *Earth. Sci. Inform.*, *3*, 41-49. doi: 10
634 .1007/s12145-010-0049-0
- 635 Filbert, P. C., & Kellogg, P. J. (1979, April). Electrostatic noise at the plasma
636 frequency beyond the earth's bow shock. *Journal of Geophysical Resarch*,
637 *84*(A4), 1369-1381. doi: 10.1029/JA084iA04p01369
- 638 Fogg, A. R., Jackman, C. M., Waters, J. E., Bonnin, X., Lamy, L., Cecconi, B., . . .
639 Louis, C. K. (2022, May). Wind/WAVES Observations of Auroral Kilometric
640 Radiation: Automated Burst Detection and Terrestrial Solar Wind - Magne-
641 tosphere Coupling Effects. *Journal of Geophysical Research (Space Physics)*,
642 *127*(5), e30209. doi: 10.1029/2021JA030209
- 643 Génot, V., Budnik, E., Jacquy, C., Bouchemit, M., Renard, B., Dufourg, N., . . .
644 Cabrolie, F. (2021, July). Automated Multi-Dataset Analysis (AMDA): An
645 on-line database and analysis tool for heliospheric and planetary plasma data.
646 *Planetary and Space Sciences*, *201*, 105214. doi: 10.1016/j.pss.2021.105214
- 647 Genova, F., Zarka, P., & Barrow, C. H. (1987, August). Voyager and Nancay obser-
648 vations of the Jovian radio-emission at different frequencies - Solar wind effect
649 and source extent. *Astronomy & Astrophysics*, *182*, 159-162.
- 650 Gurnett, D. A., Kurth, W. S., Hospodarsky, G. B., Persoon, A. M., Zarka, P.,
651 Lecacheux, A., . . . Dougherty, M. K. (2002, February). Control of Jupiter's
652 radio emission and aurorae by the solar wind. *Nature*, *415*, 985-987. doi:
653 10.1038/415985a
- 654 Gurnett, D. A., & Scarf, F. L. (1983). Physics of the Jovian magnetosphere. 8.
655 Plasma waves in the Jovian magnetosphere. In *Physics of the jovian magneto-*
656 *sphere* (p. 285-316).
- 657 Hess, S. L. G., Echer, E., & Zarka, P. (2012, September). Solar wind pressure effects
658 on Jupiter decametric radio emissions independent of Io. *Planetary Space Sci-*
659 *ence*, *70*, 114-125. doi: 10.1016/j.pss.2012.05.011
- 660 Hess, S. L. G., Echer, E., Zarka, P., Lamy, L., & Delamere, P. A. (2014, Septem-
661 ber). Multi-instrument study of the Jovian radio emissions triggered by solar
662 wind shocks and inferred magnetospheric subcorotation rates. *Planetary Space*
663 *Science*, *99*, 136-148. doi: 10.1016/j.pss.2014.05.015
- 664 Hospodarsky, G. B., Kurth, W. S., Bolton, S. J., Allegrini, F., Clark, G. B., Con-
665 nerney, J. E. P., . . . Valek, P. W. (2017, May). Jovian bow shock and magne-
666 topause encounters by the Juno spacecraft. *Geophysical Research Letters*,
667 *44*(10), 4506-4512. doi: 10.1002/2017GL073177
- 668 Imai, M., Greathouse, T. K., Kurth, W. S., Gladstone, G. R., Louis, C. K., Zarka,
669 P., . . . Connerney, J. E. P. (2019, Jan). Probing Jovian Broadband Kilo-
670 metric Radio Sources Tied to the Ultraviolet Main Auroral Oval With Juno.
671 *Geophysical Research Letters*, *46*(2), 571-579. doi: 10.1029/2018GL081227

- 672 Imai, M., Imai, K., Higgins, C. A., & Thieman, J. R. (2008, September). Angular
673 beaming model of Jupiter's decametric radio emissions based on Cassini
674 RPWS data analysis. *Geophysical Research Letters*, *35*(17), L17103. doi:
675 10.1029/2008GL034987
- 676 Imai, M., Imai, K., Higgins, C. A., & Thieman, J. R. (2011, December). Compar-
677 ison between Cassini and Voyager observations of Jupiter's decametric and
678 hectometric radio emissions. *Journal of Geophysical Research (Space Physics)*,
679 *116*(A12), A12233. doi: 10.1029/2011JA016456
- 680 Imai, M., Kurth, W. S., Hospodarsky, G. B., Bolton, S. J., Connerney, J. E. P., &
681 Levin, S. M. (2017, May). Statistical study of latitudinal beaming of Jupiter's
682 decametric radio emissions using Juno. *Geophysical Research Letters*, *44*(10),
683 4584-4590. doi: 10.1002/2017GL073148
- 684 Jackman, C. M., & Arridge, C. S. (2011, December). Solar Cycle Effects on the
685 Dynamics of Jupiter's and Saturn's Magnetospheres. *Solar Physics*, *274*(1-2),
686 481-502. doi: 10.1007/s11207-011-9748-z
- 687 Jackman, C. M., Arridge, C. S., Slavin, J. A., Milan, S. E., Lamy, L., Dougherty,
688 M. K., & Coates, A. J. (2010, October). In situ observations of the effect of
689 a solar wind compression on Saturn's magnetotail. *Journal of Geophysical*
690 *Research (Space Physics)*, *115*(A10), A10240. doi: 10.1029/2010JA015312
- 691 Jones, D. (1988, January). Planetary radio emissions from low magnetic latitudes -
692 Observations and theories. In *Planetary radio emissions ii* (p. 245-281).
- 693 Joy, S. P., Kivelson, M. G., Walker, R. J., Khurana, K. K., Russell, C. T., & Ogino,
694 T. (2002, October). Probabilistic models of the Jovian magnetopause and bow
695 shock locations. *Journal of Geophysical Research (Space Physics)*, *107*(A10),
696 1309. doi: 10.1029/2001JA009146
- 697 Khurana, K. K., Kivelson, M. G., Vasyliunas, V. M., Krupp, N., Woch, J., Lagg,
698 A., ... Kurth, W. S. (2004). The configuration of Jupiter's magnetosphere.
699 In F. Bagenal, T. E. Dowling, & W. B. McKinnon (Eds.), *Jupiter. the planet,*
700 *satellites and magnetosphere* (Vol. 1, p. 593-616).
- 701 Kilpua, E. K. J., Lumme, E., Andreeova, K., Isavnin, A., & Koskinen, H. E. J.
702 (2015). Properties and drivers of fast interplanetary shocks near the orbit
703 of the earth (19952013). *Journal of Geophysical Research: Space Physics*,
704 *120*(6), 4112-4125. Retrieved from [https://agupubs.onlinelibrary.wiley](https://agupubs.onlinelibrary.wiley.com/doi/abs/10.1002/2015JA021138)
705 [.com/doi/abs/10.1002/2015JA021138](https://agupubs.onlinelibrary.wiley.com/doi/abs/10.1002/2015JA021138) doi: [https://doi.org/10.1002/](https://doi.org/10.1002/2015JA021138)
706 [2015JA021138](https://doi.org/10.1002/2015JA021138)
- 707 Kivelson, M. G., & Khurana, K. K. (2002, August). Properties of the magnetic field
708 in the Jovian magnetotail. *Journal of Geophysical Research (Space Physics)*,
709 *107*(A8), 1196. doi: 10.1029/2001JA000249
- 710 Kurth, W. S., Hospodarsky, G. B., Kirchner, D. L., Mokrzycki, B. T., Averkamp,
711 T. F., Robison, W. T., ... Zarka, P. (2017, November). The Juno
712 Waves Investigation. *Space Science Reviews*, *213*, 347-392. doi: 10.1007/
713 s11214-017-0396-y
- 714 Ladreiter, H. P., Zarka, P., & Lacacheux, A. (1994, November). Direction finding
715 study of Jovian hectometric and broadband kilometric radio emissions: Ev-
716 idence for their auroral origin. *Planetary Space Science*, *42*, 919-931. doi:
717 10.1016/0032-0633(94)90052-3
- 718 Lamy, L., Kenfack, G., Zarka, P., Cecconi, B., Viou, c., P., R., ... A., C. (2021).
719 *Nanay Decameter Array (NDA) Jupiter Juno-Nanay data collection (Version*
720 *1.0) [Data set]*. PADC/MASER. doi: 10.25935/PBPE-BF82
- 721 Louarn, P., Allegrini, F., McComas, D. J., Valek, P. W., Kurth, W. S., André, N.,
722 ... Zink, J. L. (2017, May). Generation of the Jovian hectometric radiation:
723 First lessons from Juno. *Geophysical Research Letters*, *44*, 4439-4446. doi:
724 10.1002/2017GL072923
- 725 Louarn, P., Allegrini, F., McComas, D. J., Valek, P. W., Kurth, W. S., André, N.,
726 ... Wilson, R. J. (2018, September). Observation of Electron Conics by Juno:

- 727 Implications for Radio Generation and Acceleration Processes. *Geophysical*
728 *Research Letters*, 45(18), 9408-9416. doi: 10.1029/2018GL078973
- 729 Louarn, P., Kivelson, M. G., & Kurth, W. S. (2016, October). On the links between
730 the radio flux and magnetodisk distortions at Jupiter. *Journal of Geophysical*
731 *Research (Space Physics)*, 121(10), 9651-9670. doi: 10.1002/2016JA023106
- 732 Louarn, P., Roux, A., Perraut, S., Kurth, W., & Gurnett, D. (1998, January).
733 A study of the large-scale dynamics of the Jovian magnetosphere using the
734 Galileo Plasma Wave Experiment. *Geophysical Research Letters*, 25(15),
735 2905-2908. doi: 10.1029/98GL01774
- 736 Louis, C., Jackman, C., Mangham, S., Smith, K., O'Dwyer, E., Empey, A., ... Mal-
737 oney, S. (2022a, November). The "SPectrogram Analysis and Cataloguing
738 Environment" (SPACE) labelling tool. *Frontiers in Astronomy and Space*
739 *Sciences*, 9, 1001166. doi: 10.3389/fspas.2022.1001166
- 740 Louis, C. K., Cecconi, B., & Loh, A. (2020). *ExPRES Jovian Radio Emission Simu-*
741 *lations Data Collection (Version 01)*. PADC. doi: 10.25935/KPGE-ZB59
- 742 Louis, C. K., Hess, S. L. G., Cecconi, B., Zarka, P., Lamy, L., Aicardi, S., & Loh, A.
743 (2019, Jul). ExPRES: an Exoplanetary and Planetary Radio Emissions Simula-
744 tor. *Astronomy & Astrophysics*, 627, A30. doi: 10.1051/0004-6361/201935161
- 745 Louis, C. K., Hospodarsky, G., Jackman, C. M., O'Kane Hackett, A., Devon-Hurley,
746 E., Kurth, W. S., ... Connerney, J. E. P. (2022e). *Lists of magnetopause*
747 *and bow shock crossings, as measured by Juno/Waves and Juno/MAG (1.0.0)*
748 *[Data set]*. DIAS/Zenodo. Retrieved from [https://doi.org/10.5281/](https://doi.org/10.5281/zenodo.6460746)
749 [zenodo.6460746](https://doi.org/10.5281/zenodo.6460746) doi: 10.5281/zenodo.7304516
- 750 Louis, C. K., Jackman, C. M., Mangham, S. W., Smith, K. D., O'Dwyer, E., Empey,
751 A., ... Maloney, S. (2022b). *SPACE Labelling Tool Version 2.0.0 (v2.0.0)*
752 *[Code]*. Zenodo. doi: 10.5281/zenodo.6886528
- 753 Louis, C. K., Lamy, L., Zarka, P., Cecconi, B., Imai, M., Kurth, W. S., ... Levin,
754 S. M. (2017, September). Io-Jupiter decametric arcs observed by Juno/Waves
755 compared to ExPRES simulations. *Geophysical Research Letters*, 44, 9225-
756 9232. doi: 10.1002/2017GL073036
- 757 Louis, C. K., Prangé, R., Lamy, L., Zarka, P., Imai, M., Kurth, W. S., & Connerney,
758 J. E. P. (2019, November). Jovian Auroral Radio Sources Detected In Situ
759 by Juno/Waves: Comparisons With Model Auroral Ovals and Simultaneous
760 HST FUV Images. *Geophysical Research Letters*, 46(21), 11,606-11,614. doi:
761 10.1029/2019GL084799
- 762 Louis, C. K., Zarka, P., & Cecconi, B. (2021b). *Juno/Waves estimated flux density*
763 *Collection (Version 1.0)*. PADC/MASER. doi: 10.25935/6jg4-mk86
- 764 Louis, C. K., Zarka, P., Cecconi, B., & Kurth, W. S. (2021c). *Catalogue of Jupiter*
765 *radio emissions identified in the Juno/Waves observations (Version 1.0)*.
766 PADC/MASER. doi: 10.25935/nhb2-wy29
- 767 Louis, C. K., Zarka, P., Dabidin, K., Lampson, P. A., Magalhães, F. P., Boudouma,
768 A., ... Cecconi, B. (2021a, October). Latitudinal Beaming of Jupiter's Radio
769 Emissions From Juno/Waves Flux Density Measurements. *Journal of Geophys-*
770 *ical Research (Space Physics)*, 126(10), e29435. doi: 10.1029/2021JA029435
- 771 Mauk, B. H., Mitchell, D. G., McEntire, R. W., Paranicas, C. P., Roelof, E. C.,
772 Williams, D. J., ... Lagg, A. (2004, September). Energetic ion characteristics
773 and neutral gas interactions in Jupiter's magnetosphere. *Journal of Geophys-*
774 *ical Research (Space Physics)*, 109(A9), A09S12. doi: 10.1029/2003JA010270
- 775 McComas, D. J., Alexander, N., Allegrini, F., Bagenal, F., Beebe, C., Clark, G., ...
776 White, D. (2017, November). The Jovian Auroral Distributions Experiment
777 (JADE) on the Juno Mission to Jupiter. *Space Science Reviews*, 213, 547-643.
778 doi: 10.1007/s11214-013-9990-9
- 779 Michael, A. T., Sorathia, K. A., Merkin, V. G., Nykyri, K., Burkholder, B., Ma, X.,
780 ... Garretson, J. (2021, October). Modeling Kelvin-Helmholtz Instability
781 at the High-Latitude Boundary Layer in a Global Magnetosphere Simulation.

- 782 *Geophysical Research Letters*, 48(19), e94002. doi: 10.1029/2021GL094002
- 783 Montgomery, J., Ebert, R. W., Clark, G., Fuselier, S. A., Allegrini, F., Bagenal, F.,
784 ... Wilson, R. J. (2022, July). Investigating the Occurrence of Magnetic Re-
785 connection at Jupiter’s Dawn Magnetopause During the Juno Era. *Geophysical*
786 *Research Letters*, 49(14), e99141. doi: 10.1029/2022GL099141
- 787 Owens, M., Lang, M., Barnard, L., Riley, P., Ben-Nun, M., Scott, C. J., ... Gonzi,
788 S. (2020, March). A Computationally Efficient, Time-Dependent Model
789 of the Solar Wind for Use as a Surrogate to Three-Dimensional Numerical
790 Magnetohydrodynamic Simulations. *Solar Physics*, 295(3), 43. doi:
791 10.1007/s11207-020-01605-3
- 792 Ranquist, D. A., Bagenal, F., Wilson, R. J., Hospodarsky, G., Ebert, R. W., Al-
793 legrini, F., ... Bolton, S. J. (2019, November). Survey of Jupiter’s Dawn
794 Magnetosheath Using Juno. *Journal of Geophysical Research (Space Physics)*,
795 124(11), 9106-9123. doi: 10.1029/2019JA027382
- 796 Réville, V., Poirier, N., Kouloumvakos, A., Rouillard, A. P., Ferreira Pinto, R.,
797 Fargette, N., ... Scoul, C. (2023, March). HelioCast: heliospheric forecast-
798 ing based on white-light observations of the solar corona. *Journal of Space*
799 *Weather and Space Climate*, 13, 11. doi: 10.1051/swsc/2023008
- 800 Ronnmark, K. (1992, January). Conversion of Upper Hybrid waves into magneto-
801 spheric radiation. In *Planetary radio emissions iii* (p. 405-417).
- 802 Rouillard, A. P., Lavraud, B., Génot, V., Bouchemit, M., Dufourg, N., Plotnikov, I.,
803 ... Mays, L. (2017, November). A propagation tool to connect remote-sensing
804 observations with in-situ measurements of heliospheric structures. *Planetary*
805 *and Space Science*, 147, 61-77. doi: 10.1016/j.pss.2017.07.001
- 806 Scarf, F. L., Fredricks, R. W., Frank, L. A., & Neugebauer, M. (1971, January).
807 Nonthermal electrons and high-frequency waves in the upstream solar wind,
808 1. Observations. *Journal of Geophysical Research*, 76(22), 5162. doi:
809 10.1029/JA076i022p05162
- 810 Smith, E. J., & Wolfe, J. H. (1976, March). Observations of interaction regions and
811 corotating shocks between one and five AU: Pioneers 10 and 11. *Geophysical*
812 *Research Letters*, 3(3), 137-140. doi: 10.1029/GL003i003p00137
- 813 Tao, C., Kataoka, R., Fukunishi, H., Takahashi, Y., & Yokoyama, T. (2005, Novem-
814 ber). Magnetic field variations in the Jovian magnetotail induced by solar
815 wind dynamic pressure enhancements. *Journal of Geophysical Research (Space*
816 *Physics)*, 110(A11), A11208. doi: 10.1029/2004JA010959
- 817 Thomsen, M. F., Jackman, C. M., & Lamy, L. (2019, October). Solar Wind Dy-
818 namic Pressure Upstream From Saturn: Estimation From Magnetosheath
819 Properties and Comparison With SKR. *Journal of Geophysical Research*
820 *(Space Physics)*, 124(10), 7799-7819. doi: 10.1029/2019JA026819
- 821 Treumann, R. A. (2006, August). The electron-cyclotron maser for astrophysical ap-
822 plication. *Astronomy & Astrophysics*, 13, 229-315. doi: 10.1007/s00159-006
823 -0001-y
- 824 Tsurutani, B. T., Gonzalez, W. D., Gonzalez, A. L. C., Guarnieri, F. L., Gopal-
825 swamy, N., Grande, M., ... Vasyliunas, V. (2006, July). Corotating solar wind
826 streams and recurrent geomagnetic activity: A review. *Journal of Geophysical*
827 *Research (Space Physics)*, 111(A7), A07S01. doi: 10.1029/2005JA011273
- 828 Went, D. R., Kivelson, M. G., Achilleos, N., Arridge, C. S., & Dougherty, M. K.
829 (2011, April). Outer magnetospheric structure: Jupiter and Saturn compared.
830 *Journal of Geophysical Research (Space Physics)*, 116(A4), A04224. doi:
831 10.1029/2010JA016045
- 832 Zarka, P. (1998, September). Auroral radio emissions at the outer planets: Observa-
833 tions and theories. *Journal of Geophysical Research*, 103, 20159-20194. doi: 10
834 .1029/98JE01323
- 835 Zarka, P., & Genova, F. (1983, December). Low-frequency Jovian emission and so-
836 lar wind magnetic sector structure. *Nature*, 306(5945), 767-768. doi: 10.1038/

837 306767a0

838 Zarka, P., Magalhães, F. P., Marques, M. S., Louis, C. K., Echer, E., Lamy, L., . . .
839 Prangé, R. (2021, October). Jupiter's Auroral Radio Emissions Observed by
840 Cassini: Rotational Versus Solar Wind Control, and Components Identifica-
841 tion. *Journal of Geophysical Research (Space Physics)*, 126(10), e29780. doi:
842 10.1029/2021JA029780